Large and efficient unidirectional plane-wave–surface-wave metasurface couplers based on modulated reactance surfaces

Hakjune Lee and Do-Hoon Kwon ®*

Department of Electrical and Computer Engineering, University of Massachusetts Amherst, Amherst, Massachusetts 01003, USA

Planar metasurfaces for efficient unidirectional conversion of a plane wave into a surface wave are presented. They are designed as a reciprocal device of a decoupler or leaky-wave antenna based on spatially modulated reactance surfaces. In a surface wave-to-leaky wave conversion, the surface reactance is determined from optimization of the complete aperture field over the propagating and evanescent spectra such that the conversion surface becomes locally and globally passive and lossless, while the desired wave conversion is achieved. The coupling efficiency is given by the aperture efficiency of the reciprocal antenna, which can closely approach unity for large apertures. The optimized surface reactance is spatially discretized and translated into physical metasurfaces, comprising an array of subwavelength inclusions. In TM polarization, three lossless metasurface design examples of 40 and 80 wavelengths are provided with performance validation using full-wave simulations: a metallic groove array, a thickness-modulated grounded dielectric substrate, and a width-modulated grounded dielectric ridge array. Deviations of the surface reactance from the optimized distribution reduce the conversion efficiency, but high coupling efficiencies in excess of 98% for the metallic structure and 60% for dielectric structures are predicted.

I. INTRODUCTION

Conversion between propagating and bound states of electromagnetic waves and light is one of the fundamental functions in electromagnetic and optical engineering. In the optical regime, surface plasmon polaritons (SPPs) exist along a metal-dielectric interface as collective oscillation of free electrons [1]. At longer wavelengths, structured metallic surfaces support spoof SPPs [2]. Their propagation characteristics can be tailored by material and structural designs for a variety of applications, where high-efficiency excitation of SPPs by light is desired. To that end, unidirectional launching of SPPs upon illumination is desirable. At microwave frequencies, the reciprocal device as space-wave launchers excited by a surface wave (SW) constitutes a class of leaky-wave (LW) antennas (LWAs) [3] in antenna engineering.

Typical light-SPP converters are diffraction grating couplers and their variants [4–11], comprising a periodic or aperiodic array of metal or metal-dielectric grooves and ridges of a finite length. For maximizing the coupling efficiency and contrast ratios, the dimensions, positions, material compositions as well as specific groove profiles can be optimized. An array of gap plasmon radiators on a dielectric spacer backed by a thick gold film has also been reported [12]. The overall length is limited to a few wavelengths because the coupled waves rescatter back to free space for longer structures [11]. While inevitable loss in practical gratings prevents a perfect conversion, the theoretically maximum coupling efficiency in the absence of loss is unclear and no coupling efficiency

that closely approaches unity has been reported. For controllable coupling characteristics, tunable couplers featuring polarization-dependent SPP excitations have been investigated for circularly- [13] and linearly-polarized [14] light.

Based on the generalized Snell's law [15], Sun *et al.* [16] proposed using a phase-gradient periodic reflective metasurface for pushing the tangential wave vector of the reflected wave into the evanescent range, effectively converting an incident plane wave (PW) into an SW. This further led to the development of gradient-metasurface couplers in the optical [17,18], THz [19], and microwave [20] regimes. However, the SW that results from the anomalous reflection of the incident PW into the evanescent spectrum is not an eigenwave of the gradient metasurface, so it does not propagate a long distance before rescattering back to space, most strongly from supercell interfaces [21]. As a result, high coupling efficiency is limited to a few supercells or wavelengths. An improved solution was proposed in [22], where a transmissive phase-gradient metasurface is placed above a homogeneous (i.e., nongradient) metasurface that supports the target SW. For a metacoupler of an approximate length of 6.1 free-space wavelengths, an ideal coupling efficiency as high as 94% was predicted. We note that the transparent gradient metacoupler should be placed at a carefully controlled height, which can be challenging in practice. In addition, secondary scattering of the SW by the metacoupler results in a longitudinal wave vector pushed deeper in the evanescent range. Unless supported by the underlying homogeneous metasurface, these additional SW components will scatter back to space.

A high-efficiency coupler of a finite size based on strictly periodic metasurfaces cannot scale to much longer lengths because it cannot support a growing SW over the entire

---

*dhkwon@umass.edu

length for multiple periods. An anisotropic reflective metasurface was proposed for near-perfect conversion of a PW into a slow exponentially growing SW that can approximate a linear power growth along the coupler length [23]. An efficiency on the order of 90% was predicted for 20 wavelength-long metasurfaces and the design can scale to longer lengths. However, accurate design and realization of practical metasurfaces for the highly-inhomogeneous tensor reactance distributions are challenging. Some works proposed the physical implementation of the metasurface corresponding to the reactance over the aperture. For launching and receiving a single *inhomogeneous* PW, a periodic tensor metasurface design for exact conversion from a SW has been shown [24], followed by a scalar periodic surface reactance design suitable for printed metasurface realization [25]. Although the performance through the full-wave analysis is presented, the device is characterized by an analytical inhomogeneous reactance distribution rather than a physical structure. By placing the SW and PW on opposite sides of a penetrable metasurface, the resulting Ω-bianisotropic metasurface preserves the polarization of the incident PW in the induced SW [26]. The length of the aperture is not large, at 9.53 wavelengths at the operating frequency.

In antenna engineering, it is known that a spatially modulated impenetrable reactance surface can couple propagating and evanescent waves. In particular, the coupling principle for a sinusoidally modulated reactance surface [27] has been the basis for recent development of holographic surfaces [28] and metasurface LWAs [29,30]. Design recipes for 2D LWAs excited by cylindrical SWs capable of magnitude, phase, and polarization control have been reported [31]. Instead of working with an assumed spatial reactance profile, the complete tangential aperture fields were synthesized in finding a locally and globally passive and lossless LWA aperture that realizes desired radiation and polarization characteristics [32]. To that end, carefully chosen auxiliary SWs were added to the propagating spectral components for the aperture fields, which was originally proposed for Ω-bianisotropic metasurfaces in achieving perfect beam splitting, anomalous reflection, and field transformations using passive surfaces [33,34]. The design principle has been extended to passive impenetrable metasurfaces with tensor [35,36] and scalar [37] reactances for different applications. Such evanescent field engineering was used to design extreme asymmetry in metasurface absorption [38]. Furthermore, an LWA with controlled beam direction and leakage using a bianisotropic Huygens' metasurface was proposed and verified by measurements [39].

In this paper, metasurface PW-to-SW converters with high conversion efficiency and large contrast ratio in TM polarization are presented as reciprocal devices of planar LWAs with uniform aperture fields for broadside radiation, fed by a TM-polarized SW. A recently developed aperture field synthesis method is used to find the required surface reactance. The main contribution of this work lies in the physical designs and their performance characterization using full-wave simulations for large device dimensions. For example, 40 and 80 wavelength-long converter designs characterized by position-dependent scalar surface reactance distributions, three physical metasurfaces are designed and their coupling characteristics are analyzed using full-wave simulations. The
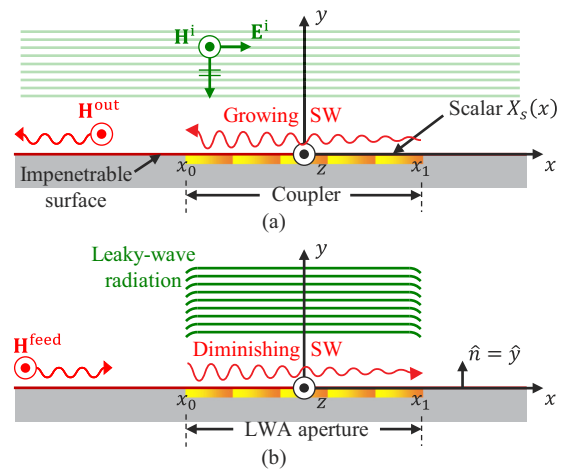

FIG. 1. A planar PW-to-SW coupler in TM polarization. (a) A coupler under a normally incident plane wave. (b) A reciprocal LWA excited by an SW, radiating a broadside beam associated with a uniform aperture field. The coupler or LWA aperture is modeled as an electromagnetically impenetrable surface characterized by a surface reactance $X_s(x)$. The configuration is uniform and invariant in z.

design technique is applicable to a coupler of arbitrary large lengths. Here, we stress that the coupling efficiency is equal to the aperture efficiency of the LWA, which has not been taken advantage of in optics when considering wave couplers. It can theoretically approach arbitrarily close to unity. Discretization of the reactance profile and inaccuracies in its realization using physical structures reduce the coupling efficiency. Still, high coupling efficiency of at least 60% is predicted for all 40 and 80 wavelength-long metasurface designs. These are large physical coupler designs with full-wave validation and their performances can serve as the baseline for large converters in the future. For modulated dielectric structures, it is found out that less-than-ideal efficiencies are due to the penetrable nature of the physical metasurface for approximating the impenetrable reactance surface.

Extensions of this work to dual-polarized couplers represented by a diagonal tensor (decoupled polarizations) or a full-tensor reactance (coupled polarizations) can be envisaged. When further combined with geometric phase control, coherent and flexible coupling control of two circular polarizations [40] may become possible with high efficiencies. It is also conceivable to design dynamically tunable or programmable converters incorporating recently demonstrated optically [41] or electrically [42] controlled diodes.

In the following time-harmonic treatment, an $e^{j\omega t}$ time dependence is assumed and suppressed.

II. COUPLER CONFIGURATION AND RECIPROCAL LWA

The PW-to-SW coupling configuration is illustrated in Fig. 1(a). A TM-polarized PW illuminates a planar coupler surface in the xy plane over $x \in [x_0, x_1]$ at normal incidence. It is desired that the power carried by the PW that falls on the coupler surface be converted unidirectionally into a TM-polarized SW propagating in the $-x$-axis direction. The

problem of a TE-polarized PW coupled to a TE-polarized SW is related to this problem by duality. The coupler is characterized by a position-dependent scalar surface reactance $X_s(x)$ of an electromagnetically impenetrable surface. We define the coupling efficiency e_{coup}, as the fraction of the PW power that is converted into the $-x$-propagating SW. The contrast ratio r_{cont}, is the ratio of the power of the $-x$-propagating SW to that of the $+x$-propagating SW away from the coupler. We aim for maximizing both e_{coup} and r_{cont} toward unity and infinity, respectively. Over $x \in [x_0, x_1]$, it is expected that a predominantly $-x$-propagating SW is induced with an increasing strength as the SW-converted power accumulates, as illustrated in Fig. 1(a). The SWs that exit the coupler surface at $x = x_0$ and x_1 propagate in the $\mp x$ directions before they are collected by SW ports located in $x < x_0$ and $x > x_1$, respectively.

The coupler in Fig. 1(a) corresponds to the receiving case of an LWA. The reciprocal transmitting case is illustrated in Fig. 1(b). The LWA is fed by a TM-polarized SW propagating in the $+x$ direction. Over the LWA aperture, the SW is continuously converted to an LW propagating in the $+y$ direction with planar wavefronts. Hence, assuming coupler design and realization using reciprocal constituents only, designing an efficient PW-to-SW coupler becomes designing an efficient LWA having a main beam in the $+y$-axis direction associated with a uniform aperture field distribution.

Furthermore, the definition of e_{coup} is exactly that of the aperture efficiency in antennas [43]. In standard cylindrical (ρ, ϕ, z) coordinates, the directivity $D_{2D}(\phi)$ of a 2D antenna is defined as

$$D_{2D}(\phi) = \frac{2\pi U(\phi)}{P_{\text{rad}}}, \tag{1}$$

where $U(\phi)$ is the radiation intensity (in W/rad) and P_{rad} is the radiated power (in W), both per unit length in z. If we denote the maximum directivity by D_0, the aperture efficiency ε_{ap} is defined as the ratio of the maximum effective width W_{em} to the physical width W_p, as appropriate for 2D antennas, as

$$\varepsilon_{\text{ap}} = \frac{W_{\text{em}}}{W_p}, \quad W_{\text{em}} = \frac{\lambda}{2\pi} D_0, \tag{2}$$

where λ is the free-space wavelength and W_p is equal to the aperture length $\ell = x_1 - x_0$ along the x direction. The coupling efficiency drops from the peak value as the angle of incidence is shifted away from $\phi^i = 90°$. The exact angular dependence is dictated by the shape of the main beam. For the uniform aperture, it is $(1 + \sin \phi) \sin(k\ell \cos \phi / 2)/(k\ell \cos \phi / 2)$. Hence, for a fixed efficiency drop, the corresponding incidence angle deviation is inversely proportional to the coupler size. For $\ell = 40\lambda$, efficiency reductions by 3 dB and 10 dB correspond to incidence angle deviations by 0.64° and 1.06°, respectively.

An ideal coupler is a lossless device that permits fabrication using passive constituents. So, the coupler design is cast into synthesis of an LWA surface with uniform aperture fields for broadside radiation that is pointwise passive and lossless everywhere. Here, the far-field requirement prescribes a uniform aperture field only over the propagating spectrum or visible region (VR). However, the surface impedance is defined in terms of the total fields over the entire spectrum

evaluated on the aperture surface. Hence, we introduce the evanescent spectrum or invisible region (IR) contents to define the complete aperture fields that render the LWA aperture locally and globally lossless, while realizing broadside radiation related to the coupling function via reciprocity.

III. MODULATED SURFACE REACTANCE SYNTHESIS

The PW-to-SW coupler design has been recast into an LWA aperture surface design modeled as an impenetrable surface. The required aperture field synthesis for different far-field characteristics has been detailed in [32]. Here, a overview of the design technique is presented together with design details for a 40λ-long converter.

In TM polarization, the E and H fields are given by $\mathbf{E} = \hat{x}E_x + \hat{y}E_y$ and $\mathbf{H} = \hat{z}H_z$. Noting that either a tangential E or H field at $y = 0$ uniquely determines $(\mathbf{E}, \mathbf{H})$ everywhere in $y \geqslant 0$, we choose to synthesize the tangential H field on the aperture, $H_{tz}(x) = H_z(x, y = 0)$. Let the field pair (E_{0x}, H_{0z}) contain the desired pattern information. We construct total the tangential H field over the aperture as

$$H_{tz}(x) = H_{0z}(x) + \underbrace{H_1(x)\,e^{-jk_c x}}_{H_{1z}(x)} + \sum_{n=2}^{N} \underbrace{H_n(x)\,e^{j(n\Delta\psi + \psi_0)}}_{H_{nz}(x)}, \tag{3}$$

for a designer-selected maximum order N, k_c chosen in the IR ($k_c > k$, $k = 2\pi/\lambda = $ free-space wavenumber) is the "carrier" phase constant or the phase constant of the feed SW. The functions $H_1(x)$ and $H_n(x)\,(n = 2, \ldots, N)$ are the envelopes for the feed SW and higher-order, fast-varying terms and $\Delta\psi(x) = -k_c x - \psi_0(x)$ with $\psi_0(x) = \angle H_{0z}(x)$. In (3), $H_1(x)$ represents a real-valued envelope for the feed SW that diminishes over the aperture. The higher-order envelopes $H_n(x)\,(n = 2, \ldots, N)$ are complex-valued, associated with spatially rapidly varying components. The associated tangential E-field, $E_{tx}(x) = E_x(x, y = 0)$, is written similarly as

$$E_{tx}(x) = E_{0x}(x) + \underbrace{E_1(x)\,e^{-jk_c x}}_{E_{1x}(x)} + \sum_{n=2}^{N} \underbrace{E_n(x)\,e^{j(n\Delta\psi + \psi_0)}}_{E_{nx}(x)}. \tag{4}$$

Each field pair $(E_{nx}, H_{nz})\,(n = 0, \ldots, N)$ as well as (E_{tx}, H_{tz}) satisfies Maxwell's equations. Therefore, each E-field component can be found from the corresponding H-field component using spatial Fourier transform relations over the x wavenumber k_x [44, Appendix B].

For a given LWA design problem, the H-field envelopes are numerically optimized such that the aperture field becomes locally and globally lossless. The first-principles condition for zero loss at an impenetrable surface point is

$$S_y(x) = -\tfrac{1}{2}\,\text{Re}\{E_{tx}(x)H_{tz}^*(x)\} = 0. \tag{5}$$

In a numerical optimization, (5) can be enforced by minimizing a relative error metric e_{sq} defined by

$$e_{\text{sq}} = \frac{1}{e_0}\int_{x_0}^{x_1} |S_y(x)|^2\,dx, \quad e_0 = \int_{x_0}^{x_1} |S_0(x)|^2\,dx, \tag{6}$$

where $S_0 = -\text{Re}\{E_{0x}H_{0z}^*\}/2$.

Once the envelopes are optimized for minimizing e_{sq} toward zero, the total tangential fields are recovered from (3) and (4). Then, the surface impedance $Z_s(x)$ that represents the
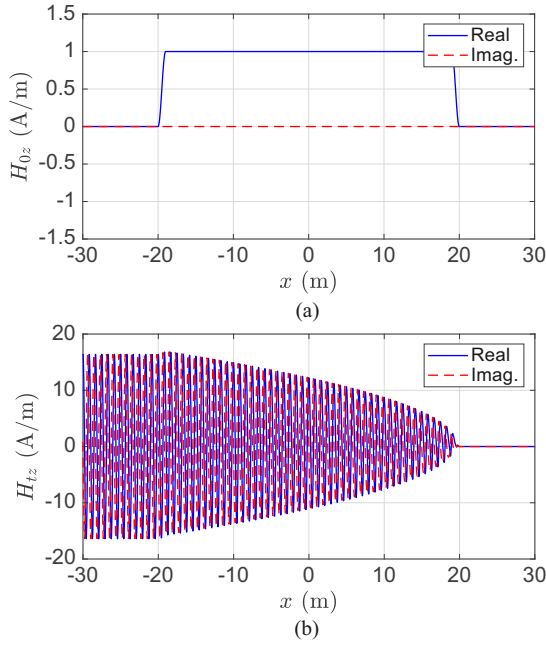
FIG. 2. Spatial H-field distributions for the 40λ-long coupler design. (a) $H_{0z}(x)$, (b) $H_{tz}(x)$.

LWA surface is found from the impedance boundary condition as

$$Z_s(x) = R_s(x) + jX_s(x) = \frac{E_{tx}(x)}{H_{tz}(x)}. \quad (7)$$

Once $R_s(x) \approx 0$ is verified, the resistance is discarded and only the surface reactance defines the aperture surface. Outside the aperture, $X_s(x)$ is set to the unmodulated value $X_{s0} = \eta\sqrt{(k_c/k)^2 - 1}$, where $\eta \approx 377\ \Omega$ is the free-space intrinsic impedance.

The field synthesis process is applied to design a 40λ-long LWA with $x_1 = -x_0 = 20\lambda$. At $f = 300$ MHz ($\lambda = 1$ m), consider a uniform aperture field specified by $H_{0z}(x) = w(x)$ A/m, where the window function $w(x)$ is equal to unity except for a raised-cosine transition to zero at each end over a distance of $D_{tr} = \lambda$. This VR aperture H field is plotted in Fig. 2(a). The radiated power is found to be $P_{rad} = 7.298$ kW/m. For determining the complete H field $H_{tz}(x)$, design parameters $N = 8$ and $k_c = 1.2k$ are chosen. Following the numerical optimization process presented in [32], the envelopes $H_n(x)$ ($n = 1, \ldots, 8$) are optimized using the *fminsearch* function for minimizing e_{sq} in MATLAB. The optimization proceeds with incrementing n by one at a time, introducing additional design parameters in each step, so that the e_{sq} is reduced until a low threshold is reached. Eventually, a total of 484 real-valued unknowns that represent sampled values of the envelopes are optimized, leading to a minimized error of $e_{sq} = 4.49 \times 10^{-5}$. The optimized total tangential H field is plotted in Fig. 2(b). For supplying the radiated power, the magnitude of the feed SW [i.e., $H_1(x)$ in $x < -20$ m] is found to be 16.40 A/m. Over the aperture, $H_{tz}(x)$ is dominated by $H_{1z}(x)$. The effect of H_{0z} in uniformly raising Re$\{H_{tz}\}$ is visible over the aperture.
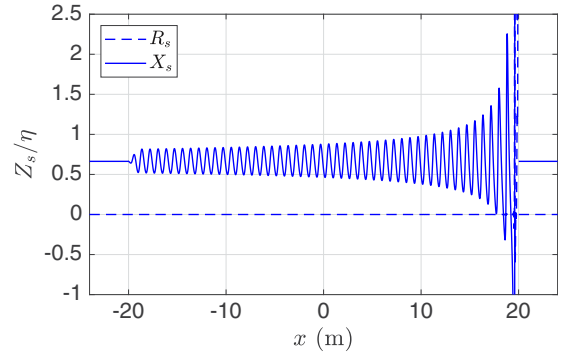

FIG. 3. The surface impedance Z_s for the 40λ-long uniform-aperture LWA normalized by η.

The retrieved surface impedance $Z_s(x)$ of the optimized design is plotted in Fig. 3. Visually, the surface resistance is brought to zero except at the end of the aperture. The surface reactance $X_s(x)$ defines the LWA or PW-to-SW coupler surface as a reactive surface. The reactance profile is close to, but different from, locally periodic sinusoidal variations [32]. It is noted that $X_s(x)$ in Fig. 3 dips below zero over two short x ranges close to $x = 20$ m.

When the surface is characterized by the impedance boundary condition with a continuously varying reactance, the resulting characteristics correspond to the ideal performance. The ideal radiation and coupling characteristics can be found using full-wave simulations by mathematically enforcing $X_s(x)$ in Fig. 3 over the surface. Figure 4 shows a snapshot of the total H-field distribution obtained using COMSOL
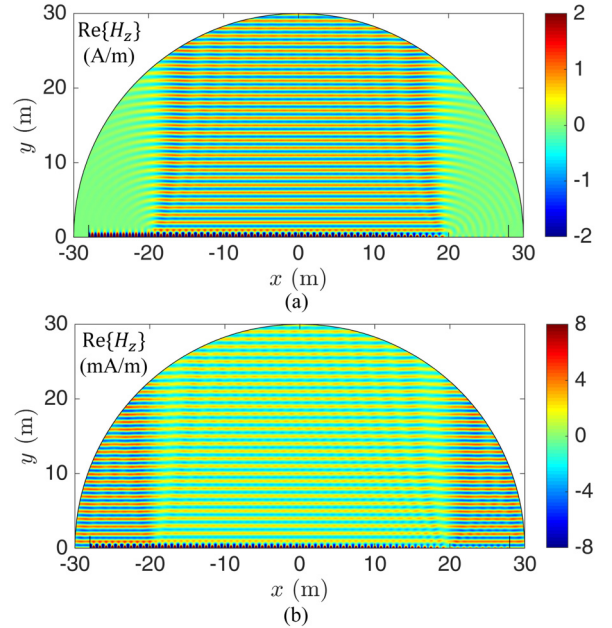

FIG. 4. Spatial field distributions of the 40λ-long coupler design. (a) Snapshot of $H_z(x, y)$ when the surface is operated as a transmitting LWA. The surface is excited by a TM SW with an incident power of 7.298 kW/m. (b) Snapshot of $H_z(x, y)$ when the surface is operated as a PW-to-SW coupler. An x-polarized unit-amplitude plane wave illuminates the surface at normal incidence.

MULTIPHYSICS, when the surface is excited by a TM SW carrying a power of $P_{rad} = 7.298$ kW/m. Ports 1 and 2 located at $x = -28\lambda$ and $x = 28\lambda$, respectively, are defined by the port H field given by $\mathbf{H}^{port} = \hat{z}e^{-\alpha_c y}$, where $\alpha_c = \sqrt{k_c^2 - k^2}$ is the attenuation constant of the feed SW in the $+y$ direction. Simulated S parameters show $|S_{11}| = -50.2$ dB and $|S_{21}| = -33.1$ dB, indicating that the transition at $x = -20\lambda$ is reflectionless and most of the input SW power is radiated away. The maximum directivity is equal to $D_0 = 23.93$ dBi at $\phi = \phi_0 = 90.0°$. Using (2), we find $W_{em} = 39.29\lambda$ and $\varepsilon_{ap} = 0.9824$.

Next, the surface is operated as a PW-to-SW coupler by illuminating it with a unit-amplitude plane wave at normal incidence having the incident E field given by $\mathbf{E}^i = \hat{x}e^{jky}$ V/m. The simulation result for the total H-field distribution is plotted in Fig. 4(b). Aside from the expected diffraction from the edge transitions at $x = \pm 20\lambda$, H_z above the aperture consists of the incident field only, indicating that the plane-wave reflection from the coupler is negligible. In fact, an SW with a growing strength with decreasing x is observed on the surface, as anticipated. Outside the coupler surface in $x < -20\lambda$ and $x > 20\lambda$, the incident wave sees a uniform unmodulated reactance surface and fully reflects, exhibiting a standing-wave pattern. The power incident on the 40λ-long surface is $P_{inc} = 53.05$ mW/m and the SW power accepted at port 1 is $P_{rx} = 52.14$ mW/m. Hence, the coupling efficiency is evaluated to be $e_{coup} = 0.9828$, which is equal to ε_{ap}. The SW coupled to the $+x$ direction is absorbed at port 2, at a power of 0.344 mW/m, giving a left-to-right contrast ratio of $r_{cont} = 151.15$.

The theoretical maximum value of the coupling efficiency is unity, associated with a uniform aperture distribution for a transmitting LWA having abrupt transitions at the two ends of the surface ($D_{tr} = 0$). A discontinuous change in the aperture field cannot be realized in practice and transitions need to be introduced. Nevertheless, using a fixed transition length D_{tr}, ε_{ap} or e_{coup} can further increase toward unity for a longer coupler length ℓ. In this context, a shorter LWA aperture of 20λ with $D_{tr} = \lambda$ gives a slightly lower aperture efficiency of 0.967 using a mathematically defined reactance surface [32].

As an example for a longer coupler, an 80λ-long coupler ($x_1 = -x_0 = 40\lambda$) is also designed using a uniform aperture and a transition with $D_{tr} = \lambda$ at both ends (not detailed). A coupling efficiency of $e_{coup} = 0.9910$ and a contrast ratio of $r_{cont} = 313.6$ are predicted.

IV. PHYSICAL METASURFACE DESIGNS

In this section, we propose three physical designs for possible realization of the impenetrable reactance surface presented in Fig. 3. They are a perfect electric conductor (PEC) groove array (a corrugated surface), a thickness-modulated grounded dielectric substrate, and a width-modulated array of grounded dielectric ridges.

A. A PEC groove array

A 2D PEC groove array or a corrugated surface is capable of supporting a TM-mode SW [45]. Figure 5(a) shows the unit cell of a PEC groove array of length or period p used
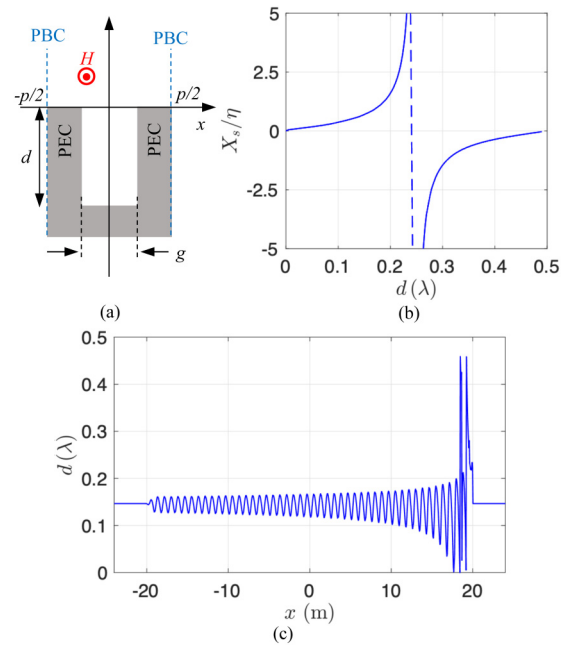

FIG. 5. PEC groove array metasurface design. (a) A unit-cell having a rectangular groove of dimensions $g \times d$ in a PEC ground in the xz plane. (b) Design curve for the surface reactance at $y = 0$ with respect to d using $p = \lambda/20$ and $g = p/2$. (c) The depth distribution for the PEC groove array metasurface along the x axis.

herein. The depth and width of a groove are given by d and g, respectively, and a groove width is chosen to be a half of the cell size ($g = p/2$). We place periodic boundary conditions (PBCs) on both sides of the cell at $x = \pm p/2$ and evaluate the reactance at the $y = 0$ surface of the PEC grooves.

As shown in Fig. 3, the designed surface impedance $Z_s(x)$ takes on both positive and negative values for the surface reactance $X_s(x)$. In order to find the relation between the groove depth d and the surface reactance $X_s(d)$ in both ranges, separate methods are employed for each range. A positive $X_s(d)$ is found using the formula $X_s(d) = \eta\sqrt{[k_x(d)/k]^2 - 1}$, where $k_x(d)$ is the propagation constant of the periodic structure along the x axis obtained using an eigenfrequency analysis in COMSOL. When it comes to a negative $X_s(d)$, it is extracted using $X_s(d) = \text{Im}\{\eta(1 + \Gamma)/(1 - \Gamma)\}$, where Γ is the reflection coefficient of a normally incident plane wave referenced at $y = 0$. As there is no conductor loss, the surface resistance $R_s(d)$ presented by the array is equal to zero. The combined design curve for $X_s(d)$ from the two methods for covering all possible reactance values is shown in Fig. 5(b).

The depth distribution of the groove array with respect to x is determined by matching the synthesized surface reactance $X_s(x)$ in Fig. 3 with the $X_s(d)$ in Fig. 5(b). The resulting depth distribution is shown in Fig. 5(c). All desired $X_s(x)$ values can be implemented within the range of $0 \leqslant d \leqslant 0.5\lambda$.

At a design frequency of $f = 300$ MHz ($\lambda = 1$ m), the conversion characteristics of the PEC groove array are numerically analyzed using COMSOL. Figure 6(a) plots a snapshot of the H-field distribution when the designed PEC groove array is operated as a PW-to-SW coupler. An unit-amplitude
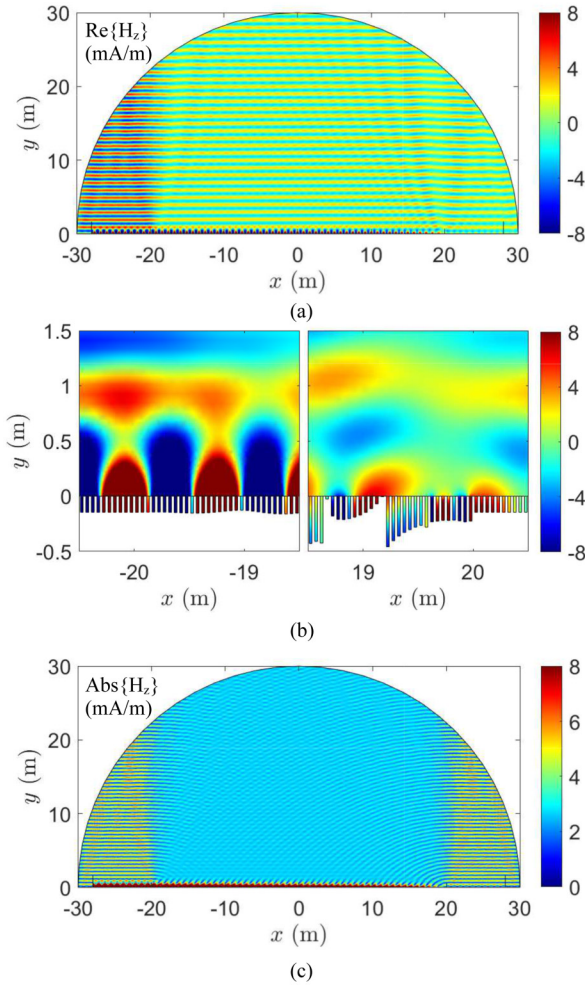
(a)

(b)

(c)

FIG. 6. PW-to-SW conversion characteristics of the 40λ-long PEC groove array metasurface. The design frequency is $f = 300$ MHz. A unit-amplitude TM-mode plane illuminates the surface from $\phi^{\mathrm{i}} = 90.19°$. (a) Snapshot of the total magnetic field $H_z(x, y)$. (b) Magnified views of $H_z(x, y)$ near the edges of the metasurface coupler, i.e., $x = -20$ m (left) and $x = 20$ m (right). (c) The magnitude distribution of the $H_z(x, y)$.

TM-mode PW is incident on the surface from the direction $\phi^{\mathrm{i}} = 90.19°$, which is the direction of maximum directivity when the surface is operated as an LWA. This maximum directivity direction is found from a separate transmit-mode simulation. The incident E field is given by $\mathbf{E}^{\mathrm{i}} = (\hat{x} \sin \phi^{\mathrm{i}} - \hat{y} \cos \phi^{\mathrm{i}}) e^{jk(x \cos \phi^{\mathrm{i}} + y \sin \phi^{\mathrm{i}})}$ V/m. Placed at $x = -28\lambda$ and 28λ, respectively, the SW ports 1 and 2 are set up using the tangential H field evaluated on the port face from the eigenwave solution of the unmodulated PEC groove array. As can be observed near the converter surface in Fig. 6(a), the incident PW is converted to an SW as in the ideal case in $x \in [-20\lambda, 20\lambda]$. From the edges of the aperture at $x = \pm 20\lambda$, where a transition occurs between unmodulated and modulated parts of the array, diffraction appear as is anticipated in Fig. 4.

Magnified views of the H-field distributions near the edges of the metasurface are plotted in Fig. 6(b), in which details of the grooves as well as the fields inside them are shown. In

particular, grooves with depth deeper than $\lambda/4$ for realizing negative reactance values are seen close to $x = 20$ m. These deep grooves play their part in achieving high conversion efficiency. Through the transition over $D_{\mathrm{tr}} = \lambda$ at $x = -20\lambda$, the accumulated $-x$-propagating SW propagates nearly without reflection to the unmodulated groove portion before being absorbed at port 1. On the other hand, a small amount of $+x$-propagating SW exits the transition at $x = 20\lambda$ before being received at port 2.

Figure 6(a) shows weak total field in $x > 20\lambda$ compared with the left of the metasurface in $x < -20\lambda$. This is because what is shown in Fig. 6(a) is a field snapshot, combined with the fact that the incident wave direction is not exactly normal to the surface. The H-field magnitude is plotted in Fig. 6(c) and standing-wave patterns are visible on both sides with similar magnitudes. From simulation, the coupling efficiency e_{coup} of the PEC groove array is evaluated to be 0.9860, which shows a good match with the ideal performance. In addition, a high left-to-right contrast ratio of $r_{\mathrm{cont}} = 201.6$ is found.

In case of the 80λ-long PEC groove array designed in the same fashion, it is able to receive a plane wave most efficiently from $\phi^{\mathrm{i}} = 90.19°$ with an efficiency of $e_{\mathrm{coup}} = 0.9843$, which is close to the high predicted value. The contrast ratio r_{cont} is equal to 93.36. The results for 40λ- and 80λ-long arrays show that a large PEC groove array is capable of achieving the high coupling efficiency predicted by the modulated surface reactance.

A PEC groove array may be accurately realized at microwave frequencies as a corrugated metallic surface owing to low conductor loss and available precision machining techniques.

B. A thickness-modulated grounded dielectric substrate

At higher frequencies toward the optical regime, a dielectric metasurface is preferred to predominantly metallic structures. A depth-modulated grounded dielectric substrate consists of dielectric cells on a PEC ground whose thickness is continuously varied. The configuration of a dielectric coated PEC ground with a dielectric of thickness or depth d and a relative permittivity ϵ_r is illustrated in Fig. 7(a). Here, we choose to keep the top surface of the dielectric layer planar at $y = 0$ and modulate the y coordinate of the ground to realize a given surface reactance at $y = 0$. It is also possible to choose a planar ground and change the shape of the dielectric-free space interface. The fields of the TM (to x) mode inside and outside the dielectric are analytically given as follows [45]:

$$H_z(x, y) = -Aue^{-jk_x x} \cos uy, \tag{8}$$

$$E_x(x, y) = \frac{\eta A}{jk\epsilon_r} u^2 e^{-jk_x x} \sin uy, \tag{9}$$

in $-d \leqslant y < 0$ and

$$H_z(x, y) = Bve^{-jk_x x} e^{vy}, \tag{10}$$

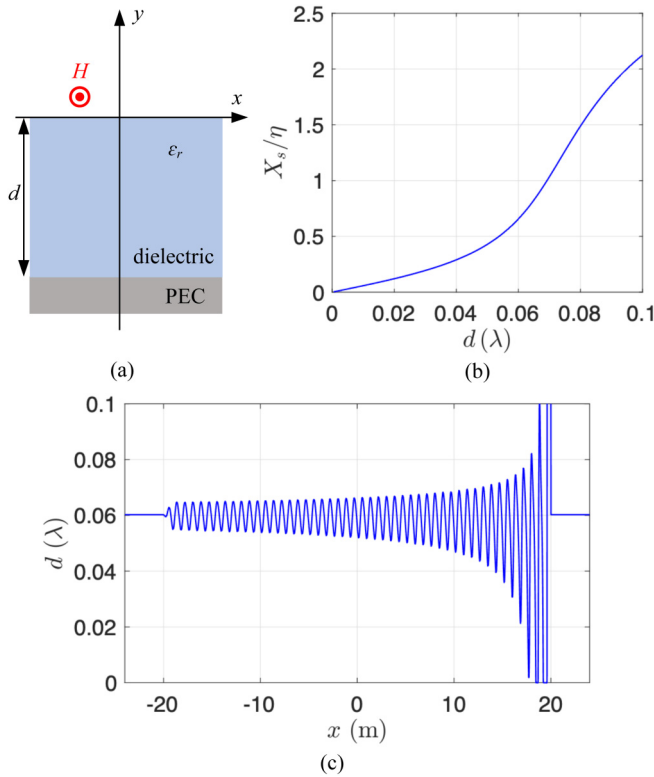$$E_x(x, y) = -\frac{\eta B}{jk} v^2 e^{-jk_x x} e^{vy}, \tag{11}$$

(a)

(b)

FIG. 7. Thickness-modulated grounded dielectric substrate metasurface design. (a) A dielectric substrate of thickness d and a relative permittivity ϵ_r on a PEC ground. (b) Design curve for the surface reactance at $y = 0$ with respect to d when $\epsilon_r = 11$. (c) The thickness distribution of the 40λ-long thickness-modulated dielectric substrate metasurface.

in $y \geqslant 0$ in terms of some constants A and B, where $u = \sqrt{k^2 \epsilon_r - k_x^2}$ and $v = j\sqrt{k^2 - k_x^2}$ are the wavenumbers along the y axis inside and outside the dielectric, respectively. There is a nonzero normal E-field component, but it does not affect the surface impedance at $y = 0$. Requiring the continuity of tangential fields at $y = 0$ using (8)–(11), the dielectric thickness d can be found for a given surface reactance $X_s(x)$ by numerically solving

$$u^2 + \left(\frac{k}{\eta} X_s\right)^2 = k^2(\epsilon_r - 1), \quad (12)$$

$$d = \frac{1}{u} \tan^{-1}\left(\frac{k\epsilon_r X_s}{\eta u}\right). \quad (13)$$

For a dielectric with $\epsilon_r = 11$ (close to that of silicon), the retrieved relation between d and X_s is plotted in Fig. 7(b). The maximum thickness of the dielectric is chosen to be 0.1λ to cover most of the designed surface reactance $X_s(x)$. The maximum achievable reactance levels off quickly beyond $d = 0.1\lambda$. In the range $d \in [0, 0.1\lambda]$, the surface reactance presented at $y = 0$ is limited to $X_s < 2.12\eta = 801$ Ω. Unlike in the PEC groove array, negative surface reactance is not available. Hence, values of the synthesized surface reactance above 801 Ω and below 0 Ω are set to 801 Ω and 0 Ω, respectively. The resulting dielectric thickness profile for
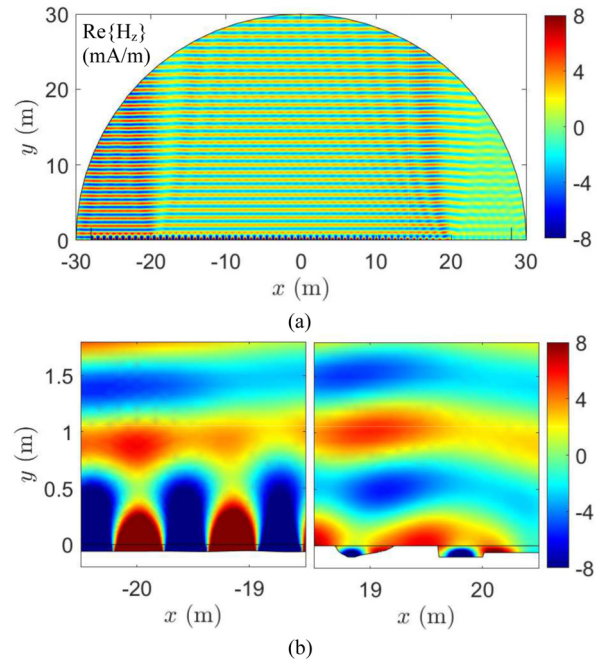

(a)

(b)

FIG. 8. PW-to-SW conversion characteristics of the 40λ-long thickness-modulated grounded substrate metasurface at $f = 300$ MHz. A unit-amplitude TM-mode plane illuminates the surface from the direction $\phi^i = 90.2°$. (a) Snapshot of the total magnetic field $H_z(x, y)$. (b) Magnified views of $H_z(x, y)$ over the transition regions of the metasurface coupler near $x = -20$ m (left) and $x = 20$ m (right).

the range-limited surface reactance distribution is shown in Fig. 7(c).

Defined by a continuously-varying thickness d with respect to x, we arrive at a 40λ-long, 2D physical metasurface design at $f = 300$ MHz. Its wave conversion performance is numerically tested using COMSOL. In the same way as for the PEC groove structure, the illuminating angle is determined to be $\phi^i = 90.2°$ as the direction of maximum directivity when the metasurfaces radiates as a transmitting antenna. The SW ports located at $x = -28\lambda$ and 28λ are configured to accept the fields in (8)–(11). Simulation results in a receiving operation are shown in Fig. 8. A snapshot of the total H-field distribution shown in Fig. 8(a) indicates that the incident PW is transformed into an SW over the modulated surface over $x \in [-20\lambda, 20\lambda]$, exhibiting a similar behavior as in Fig. 4(b). However, the scattered fields are stronger than in the ideal case from the two ends of the modulated surface, especially near $x = 20\lambda$.

Magnified views of the H-field distribution are shown in Fig. 8(b) near the beginning and end of the converter surface. Over most of the converter length, the thickness d changes smoothly with respect to x. However, the inability to synthesize negative surface values near the end of the aperture causes abrupt thickness changes, which appears to be the origin of the strong scattering near $x = 20\lambda$ [cf. Fig. 6(b)]. Nevertheless, a strong $-x$-propagating SW is established, as can be seen near $x = -20\lambda$ in Fig. 8(b). The coupling efficiency of the metasurface is found to be $e_{\mathrm{coup}} = 0.8120$, which is lower than
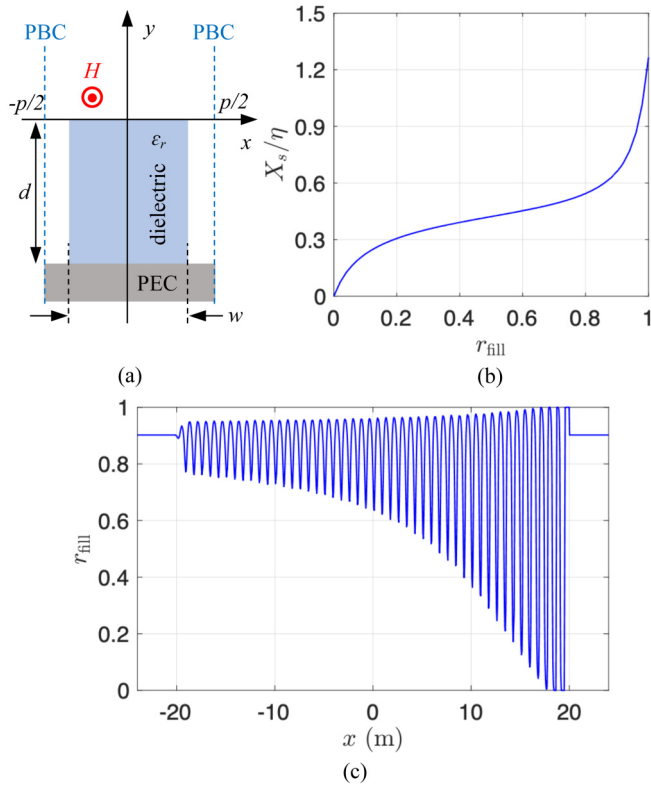
(a)

(b)

(c)

FIG. 9. Width-modulated grounded dielectric ridge array design. (a) Unit cell of a dielectric ridge of dimensions $w \times d$ and relative permittivity ϵ_r on a PEC ground in the $y = -d$ plane. (b) Design curve for the surface reactance at $y = 0$ with respect to the fill factor $r_{\text{fill}} = w/p$ when $p = \lambda/20$, $d = 0.075\lambda$, and $\epsilon_r = 11$. (c) The distribution of r_{fill} of the dielectric ridge array metasurface with respect to x for the 40λ-long coupler.

the ideal case as well as the PEC groove metasurface. The reduced coupling efficiency may be attributed to the limited synthesizable reactance range and the penetrable nature of the $y = 0$ surface in this design. Coupling between neighboring cells having different dielectric thicknesses is obviously stronger than in PEC grooves. The left-to-right contrast ratio is evaluated to be high at $r_{\text{cont}} = 478.51$.

The 80λ-long thickness-modulated aperture acts as a PW-to-SW converter with similar performance to the 40λ-aperture design. The incidence direction where the maximum efficiency occurs is $\phi^i = 90.1°$. The coupling efficiency and contrast ratio slightly increase to $e_{\text{coup}} = 0.8237$ and $r_{\text{cont}} = 589.45$, respectively.

C. A width-modulated grounded dielectric ridge array

A second metasurface based on modulation of a dielectric constituent is an array of width-modulated grounded dielectric ridges. Figure 9(a) illustrates the unit cell of length p that contains a dielectric ridge of width w and a fixed thickness d on a PEC ground plane. The relative permittivity of the dielectric is ϵ_r and PBCs are applied at $x = \pm p/2$ for unit-cell analysis to retrieve the surface reactance presented in the $y = 0$ plane. The surface reactance is modulated by changing the extent of
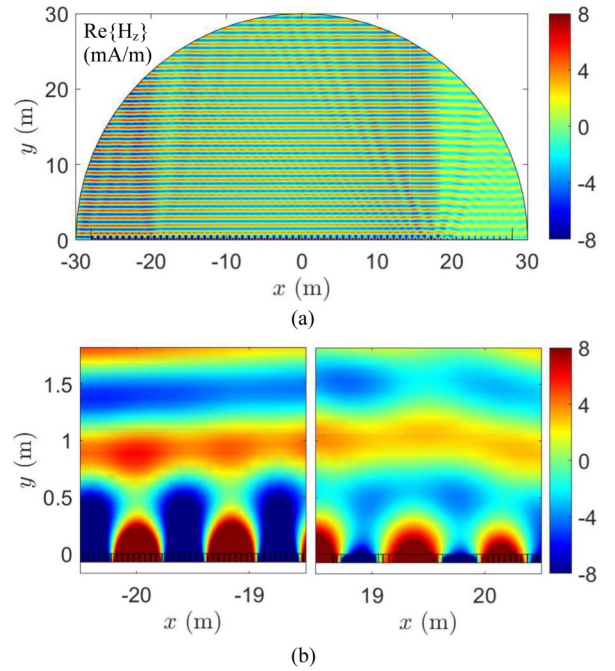

(a)

(b)

FIG. 10. PW-to-SW conversion characteristics of the 40λ-long width-modulated dielectric ridge metasurface at $f = 300$ MHz. A unit-amplitude TM-mode plane wave illuminates the surface from the $\phi^i = 90.21°$. (a) Snapshot of the total magnetic field $H_z(x, y)$. (b) Magnified views of $H_z(x, y)$ near the metasurface coupler edges at $x = -20$ m (left) and $x = 20$ m (right).

the dielectric inside the unit cell, quantified by the fill factor or fill ratio $r_{\text{fill}} = w/p$. In this design, we choose $p = \lambda/20$, $d = 0.075\lambda$, and $\epsilon_r = 11$. The dielectric thickness d is fixed at 0.075λ in order to avoid the undesired modes from being excited for thick dielectric ridges, while covering most of the designed surface reactance $X_s(x)$. Owing to the electrically small cell size ($p \ll \lambda$), a width-modulated dielectric ridge array would look like a dielectric coated ground plane with varying effective permittivity for a wave propagating along the x axis. This allows TM-polarized SWs to propagate over the structure. For the unit cell in Fig. 9(a), we obtain the surface reactance at $y = 0$ using COMSOL eigenfrequency analysis. The surface reactance presented by the unit cell at $y = 0$ is obtained by field averaging, i.e., by taking a ratio between the x-averaged value of $E_x(x, y = 0)$ and that of $H_z(x, y = 0)$ over the entire cell length. The resulting design curve is shown in Fig. 9(b). The homogenized surface reactance is a monotonically increasing function of r_{fill}. The maximum surface reactance being able to realize is equal to $1.27\eta = 477.2 \ \Omega$.

Using the design curve for the fill factor in Fig. 9(b), we obtain the fill factor profile shown in Fig. 9(c) for the 40λ-long coupler. Due to the limited range of realizable reactance, the ideal surface reactance profile in Fig. 3 is effectively clipped at 0 and 1.27η in this metasurface design.

The coupling characteristics of the metasurface are simulated using COMSOL. Subject to a unit plane-wave illumination, the total H-field distribution is plotted in Fig. 10(a). The direction of the incident wave is $\phi^i = 90.21°$, obtained via the same process as for the previous structures. SW ports 1 and
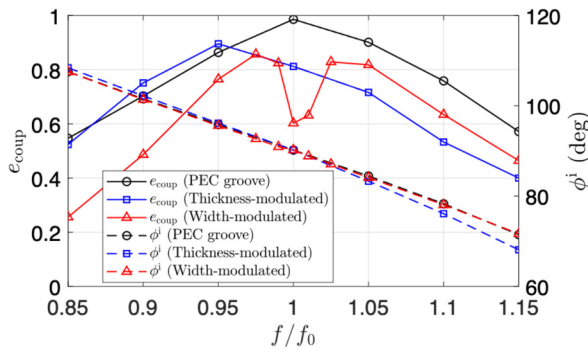
FIG. 11. The coupling efficiency and the associated direction of incidence with respect to the normalized frequency for the three 40λ physical coupler designs.

2 placed at $x = -28\lambda$ and 28λ are defined by the tangential E-field distribution on the periodic boundaries at $x = \pm p/2$ extracted from the COMSOL eigenfrequency simulation. In comparison with the previous structures, Fig. 10(a) shows that a stronger SW propagates in the $+x$-axis direction to the right side of the metasurface before being absorbed at port 2. This can be mainly attributed to the clipping of the reactance range to $X_s \in [0, 1.27\eta]$ near $x = 20\lambda$. A strongly asymmetric SW excitation—the $-x$-propagating SW being stronger than the $+x$-propagating SW—is due to the oscillation of $X_s(x)$ in Fig. 3 with larger swings as x increases. Due to the clipping of X_s, this increasing reactance swing is not realized near the end of the converter [see r_{fill} reaching zero and unity a few times near $x = 20$ m in Fig. 9(c)], ending up exciting a $+x$-propagating SW of a nonnegligible magnitude.

Magnified views of the H-field distribution are shown in Fig. 10(b), where the ridge array geometry as well as the fields inside and outside the dielectric are detailed. Difference in fields from the two previous metasurfaces shown in Figs. 6(b) and 8(b) can be observed, including a noticeable SW strength near $x = 20$ m. As a result, the contrast ratio is not high, at $r_{\text{cont}} = 10.65$. The coupling efficiency of the width-modulated dielectric ridge array is found to be $e_{\text{coup}} = 0.6024$, lower than for the previous metasurface designs. The main reasons of the reduced efficiency are use of a physically penetrable surface at $y = 0$ for realizing a surface modeled as an impenetrable surface and a limited range of achievable surface reactance available in the chosen physical configuration. It was observed that SW propagation through the λ-wide transition at $x = -20$ m suffers reflection, which was not observed for the PEC groove array and not significant for the thickness-modulated substrate.

Like the previous structure, the width-modulated dielectric ridge array of a 80λ length maintain its performance compared with the 40λ-design. The incidence direction of maximum efficiency is $\phi^i = 89.9°$. Slightly larger coupling efficiency $e_{\text{coup}} = 0.6240$ and contrast ratio $r_{\text{cont}} = 23.596$ are obtained.

Lastly, the bandwidth property is numerically tested for the 40λ-long couplers. The angle of incidence for maximum coupling is a strong function of frequency. Figure 11 plots e_{coup}, given by the LWA aperture efficiency, with respect to frequency together the associated incidence angle ϕ^i. For the

PEC groove array, e_{coup} decreases as the frequency moves away from the design frequency $f_0 = 300$ MHz. For the thickness-modulated substrate and the width-modulated ridge array, we cannot anticipate with certainty that e_{coup} will be maximum at f_0 and monotonically decrease as frequency changes, because these structures are penetrable at $y = 0$ while the synthesized reactance represents an impenetrable surface. In fact, the width-modulated ridge array has a dip in efficiency at the design frequency. In contrast to the PEC groove array, they allow power flow in the longitudinal direction below the $y = 0$ surface. We recognize this penetrable nature of dielectric designs as the main cause for suboptimal performance. The angle of maximum efficiency for all three structures changes similarly with frequency. Over the frequency range tested, ϕ^i varies from $110°$ to around $70°$.

V. CONCLUSIONS

Planar metasurface designs for efficient and unidirectional conversion of a PW into an SW have been presented, which are equivalent to planar leaky-wave antennas comprising reciprocal constituents excited by a feeding SW operating in a receiving configuration. The converter surface is modeled as an electromagnetically impenetrable surface with a position-dependent surface impedance. In an SW-to-LW conversion operation as a transmitting antenna, complete surface fields over both the propagating and evanescent spectra are determined such that the converter surface becomes passive and lossless everywhere, while the desired wave conversion is performed. The coupling efficiency is equal to the antenna aperture efficiency. Physical metasurfaces can be designed to realize the synthesized surface reactance distribution.

An optimal surface reactance profile has been synthesized for 40λ- and 80λ-long 2D metasurface couplers and three physical metasurface design examples have been presented. A PEC groove array design may be accurately approximated by a corrugated metallic surface at microwave frequencies. A thickness-modulated grounded dielectric metasurface and a width-modulated grounded dielectric ridge array metasurface are more suitable at higher frequencies toward the optical regime. Full-wave simulations show that a coupling efficiency as high as 98% that matches the ideal efficiency is predicted for the perfect conductor structure. For modulated-dielectric designs, coupling efficiencies in excess of 60% are predicted for 40λ- and 80λ-long apertures. Main reasons for the reduced efficiency for modulated dielectric metasurfaces are the penetrable nature of the dielectric medium with the ambient space and the strong coupling that takes place in the longitudinal direction below the coupler surface. We believe that the proposed metasurface structures and their refinements will find applications in efficient electronic, plasmonic, and photonic devices that rely on controlled interaction between bound waves and space waves.

[1] S. A. Maier, *Plasmonics: Fundamentals and Applications* (Springer, New York, 2007).

[2] J. B. Pendry, L. Martín-Moreno, and F. J. Garcia-Vidal, Mimicking surface plasmons with structured surfaces, Science **305**, 847 (2004).

[3] A. A. Oliner and D. R. Jackson, Leaky-wave antennas, in *Antenna Engineering Handbook*, edited by J. L. Volakis (McGraw Hill, New York, 2007), Chap. 11.

[4] F. López-Tejeira, S. G. Rodrigo, L. Martín-Moreno, F. J. García-Vidal, E. Devaux, T. W. Ebbesen, J. R. Krenn, I. P. Radko, S. I. Bozhevolnyi, M. U. González, J. C. Weeber, and A. Dereux, Efficient unidirectional nanoslit couplers for surface plasmons, Nat. Phys. **3**, 324 (2007).

[5] J. Lu, C. Petre, and E. Yablonovitch, Numerical optimization of a grating coupler for the efficient excitation of surface plasmons at an Ag-SiO$_2$ interface, J. Opt. Soc. Am. B **24**, 2268 (2007).

[6] J. Andkjær, S. Nishiwaki, T. Nomura, and O. Sigmund, Topology optimization of grating couplers for the efficient excitation of surface plasmons, J. Opt. Soc. Am. B **27**, 1828 (2010).

[7] I. P. Radko, S. I. Bozhevolnyi, G. Brucoli, L. Martín-Moreno, F. J. García-Vidal, and A. Boltasseva, Efficient unidirectional ridge excitation of surface plasmons, Opt. Express **17**, 7228 (2009).

[8] A. Baron, E. Devaux, J.-C. Rodier, J.-P. Hugonin, E. Rousseau, C. Genet, T. W. Ebbesen, and P. Lalanne, Compact antenna for efficient and unidirectional launching and decoupling of surface plasmons, Nano Lett. **11**, 4207 (2011).

[9] S. T. Koev, A. Agrawal, H. J. Lezec, and V. A. Aksyuk, An efficient large-area grating coupler for surface plasmon polaritons, Plasmonics **7**, 269 (2012).

[10] X. Huang and M. L. Brongersma, Compact aperiodic metallic groove arrays for unidirectional launching of surface plasmons, Nano Lett. **13**, 5420 (2013).

[11] T. Liu, Y. Shen, W. Shin, Q. Zhu, S. Fan, and C. Jin, Dislocated double-layer metal gratings: An efficient unidirectional coupler, Nano Lett. **14**, 3848 (2014).

[12] Z. Lei and T. Yang, Gap plasmon resonator arrays for unidirectional launching and shaping of surface plasmon polaritons, Appl. Phys. Lett. **108**, 161105 (2016).

[13] J. Lin, J. P. Balthasar Mueller, Q. Wang, G. Yuan, N. Antoniou, X.-C. Yuan, and F. Capasso, Polarization-controlled tunable directional coupling of surface plasmon polaritons, Science **340**, 331 (2013).

[14] A. Pors, M. G. Nielsen, T. Bernardin, J.-C. Weeber, and S. I. Bozhevolnyi, Efficient unidirectional polarization-controlled excitation of surface plasmon polaritons, Light: Sci. Appl. **3**, e197 (2014).

[15] N. Yu, P. Genevet, M. A. Kats, F. Aieta, J.-P. Tetienne, F. Capasso, and Z. Gaburro, Light propagation with phase discontinuities: Generalized laws of reflection and refraction, Science **334**, 333 (2011).

[16] S. Sun, Q. He, S. Xiao, Q. Xu, X. Li, and L. Zhou, Gradient-index meta-surfaces as a bridge linking propagating waves and surface waves, Nat. Mater. **11**, 426 (2012).

[17] S. Sun, K.-Y. Yang, C.-M. Wang, T.-K. Juan, W. T. Chen, C. Y. Liao, Q. He, S. Xiao, W.-T. Kung, G.-Y. Guo, L. Zhou, and D. P. Tsai, High-efficiency broadband anomalous reflection by gradient meta-surfaces, Nano Lett. **12**, 6223 (2012).

[18] C. Gong, J. Zhang, and S. He, Hybrid unidirectional metacoupler for vertical incidence to a high-refractive-index waveguide in telecom wavelength, Opt. Lett. **42**, 5098 (2017).

[19] L.-Z. Yin, T.-J. Huang, F.-Y. Han, J.-Y. Liu, D. Wang, and P.-K. Liu, High-efficiency terahertz spin-decoupled metacoupler for spoof surface plasmon excitation and beam steering, Opt. Express **27**, 18928 (2019).

[20] J. Duan, H. Guo, S. Dong, T. Cai, W. Luo, Z. Liang, Q. He, L. Zhou, and S. Sun, High-efficiency chirality-modulated spoof surface plasmon metacoupler, Sci. Rep. **7**, 1354 (2017).

[21] C. Qu, S. Xiao, S. Sun, Q. He, and L. Zhou, A theoretical study on the conversion efficiencies of gradient metasurfaces, EPL **101**, 54002 (2013).

[22] W. Sun, Q. He, S. Sun, and L. Zhou, High-efficiency surface plasmon meta-couplers: Concept and microwave-regime realizations, Light: Sci. Appl. **5**, e16003 (2016).

[23] S. N. Tcvetkova, D.-H. Kwon, A. Díaz-Rubio, and S. A. Tretyakov, Near-perfect conversion of a propagating plane wave into a surface wave using metasurfaces, Phys. Rev. B **97**, 115447 (2018).

[24] S. N. Tcvetkova, S. Maci, and S. A. Tretyakov, Exact solution for conversion of surface waves to space waves by periodical impenetrable metasurfaces, IEEE Trans. Antennas Propag. **67**, 3200 (2019).

[25] S. N. Tcvetkova, E. Martini, S. A. Tretyakov, and S. Maci, Perfect conversion of a TM surface wave into a TM leaky wave by an isotropic periodic metasurface printed on a grounded dielectric slab, IEEE Trans. Antennas Propag. **68**, 6145 (2020).

[26] V. Popov, A. Díaz-Rubio, V. Asadchy, S. Tcvetkova, F. Boust, S. Tretyakov, and S. N. Burokur, Omega-bianisotropic metasurface for converting a propagating wave into a surface wave, Phys. Rev. B **100**, 125103 (2019).

[27] A. A. Oliner and A. Hessel, Guided waves on sinusoidally-modulated reactance surfaces, IRE Trans. Antennas Propag. **7**, 201 (1959).

[28] B. H. Fong, J. S. Colburn, J. J. Ottusch, J. L. Visher, and D. F. Sievenpiper, Scalar and tensor holographic artificial impedance surfaces, IEEE Trans. Antennas Propag. **58**, 3212 (2010).

[29] A. M. Patel and A. Grbic, A printed leaky-wave antenna based on a sinusoidally-modulated reactance surface, IEEE Trans. Antennas Propag. **59**, 2087 (2011).

[30] G. Minatti, D. González-Ovejero, E. Martini, and S. Maci, Modulated metasurface antennas, in *Surface Electromagnetics: With Applications in Antenna, Microwave, and Optical Engineering*, edited by F. Yang and Y. Rahmat-Samii (Cambridge University Press, Cambridge, 2019), Chap. 7.

[31] G. Minatti, F. Caminita, E. Martini, M. Sabbadini, and S. Maci, Synthesis of modulated-metasurface antennas with amplitude, phase, and polarization control, IEEE Trans. Antennas Propag. **64**, 3907 (2016).

[32] D.-H. Kwon, Modulated reactance surfaces for leaky-wave radiation based on complete aperture field synthesis, IEEE Trans. Antennas Propag. **68**, 5463 (2020).

[33] A. Epstein and G. V. Eleftheriades, Synthesis of Passive Lossless Metasurfaces Using Auxiliary Fields for Reflectionless Beam Splitting and Perfect Reflection, Phys. Rev. Lett. **117**, 256103 (2016).

[34] A. Epstein and G. V. Eleftheriades, Arbitrary power-conserving field transformations with passive lossless omega-type bian-isotropic metasurfaces, IEEE Trans. Antennas Propag. **64**, 3880 (2016).

[35] D.-H. Kwon, Lossless tensor surface electromagnetic cloaking for large objects in free space, Phys. Rev. B **98**, 125137 (2018).

[36] D.-H. Kwon, Illusion electromagnetics for free-standing objects using passive lossless metasurfaces, Phys. Rev. B **101**, 235135 (2020).

[37] D.-H. Kwon, Lossless scalar metasurfaces for anomalous reflection based on efficient surface field optimization, IEEE Antennas Wireless Propag. Lett. **17**, 1149 (2018).

[38] X. Wang, A. Díaz-Rubio, V. S. Asadchy, G. Ptitcyn, A. A. Generalov, J. Ala-Laurinaho, and S. A. Tretyakov, Extreme Asymmetry in Metasurfaces Via Evanescent Fields Engineering: Angular-Asymmetric Absorption, Phys. Rev. Lett. **121**, 256802 (2018).

[39] E. Abdo-Sánchez, M. Chen, A. Epstein and G. V. Eleftheriades, A leaky-wave antenna with controlled radiation using a bian-isotropic Huygens' metasurface, IEEE Trans. Antennas Propag. **67**, 108 (2019).

[40] S. Xiao, F. Zhong, H. Liu, S. Zhu, and J. Li, Flexible coherent control of plasmonic spin-hall effect, Nat. Commun. **6**, 8360 (2015).

[41] X. G. Zhang, W. X. Jiang, H. L. Jiang, Q. Wang, H. W. Tian, L. Bai, Z. J. Luo, S. Sun, Y. Luo, C.-W. Qiu, and T. J. Cui, An optically driven digital metasurface for programming electromagnetic functions, Nat. Electron. **3**, 165 (2020).

[42] Y. Li, J. Lin, H. Guo, W. Sun, S. Xiao, and L. Zhou, A tunable metasurface with switchable functionalities: From perfect transparency to perfect absorption, Adv. Opt. Mater. **8**, 1901548 (2020).

[43] C. A. Balanis, *Antenna Theory: Analysis and Design*, 4th ed. (Wiley, Hoboken, NJ, 2016).

[44] D.-H. Kwon and S. A. Tretyakov, Arbitrary beam control using passive lossless metasurfaces enabled by orthogonally polarized custom surface waves, Phys. Rev. B **97**, 035439 (2018).

[45] R. F. Harrington, *Time-Harmonic Electromagnetic Fields* (IEEE Press, Piscataway, NJ, 2001).